

# Bistatic Scattering and Emissivities of Lossy Dielectric Surfaces With Exponential Correlation Functions

Peng Xu and Leung Tsang, *Fellow, IEEE*

**Abstract**—Bistatic scattering and emissivities of surfaces with exponential correlation functions are studied numerically for 2-D geometries in a numerical Maxwell model with 2-D simulations. Surfaces with exponential correlation functions are important for the active and passive microwave remote sensing of land surfaces. Because of the fine-scale features with large slopes of such surfaces, numerical accuracy, which is particularly important for the calculation of emissivity in passive remote sensing, is ensured by a variety of procedures in this paper. The rooftop function and Galerkin's method with numerical integration of near-field impedance matrix elements are used. Cubic spline interpolation is employed to connect knots on random rough surfaces. Numerical accuracy convergence tests are performed for numerical solutions of Maxwell equations by varying the number of points from 13 to 103 points per wavelength in the dielectric medium corresponding to 50–400 points per free wavelength. Surface lengths of up to 100 and 200 free wavelengths and root mean square heights of up to 0.4 and 0.8 free wavelengths, respectively, are used at 5 and 10 GHz to capture all the essential features. Because of the large number of surface unknowns (up to 80 000), the multilevel UV method is further used to accelerate the matrix equation solver. Numerical results are illustrated for both bistatic scattering and emissivities as functions of frequencies and incidence and scattering angles for cases of interests in microwave remote sensing. Comparisons are made with the second-order small perturbation method and Kirchhoff's approximation to reestablish the regimes of validity of these methods.

**Index Terms**—Active remote sensing, electromagnetic scattering, fast solver, microwave emissivity, passive remote sensing, soil rough surface.

## I. INTRODUCTION

IN MICROWAVE remote sensing of land surfaces, surfaces with exponential correlation functions have become a common choice in recent years. The use of a Gaussian correlation function is not appropriate for land surfaces. Natural surfaces can have different types of correlation functions. There is also the presence of vegetation, rocks, etc. However, exponential correlations appear to match experimental data much better than Gaussian correlation functions [1]. In this paper, we report on the differences of active and passive

microwave remote signatures between Gaussian correlation function surfaces and exponential correlation function surfaces. Surfaces with exponential correlation functions have fine-scale features that are more irregular than that of a Gaussian correlation function of the same root mean square (rms) height and correlation length [2]. In the past, the small perturbation method (SPM) and Kirchhoff's approximation (KA) have been widely applied in rough surface scattering. Regimes of validity were established for these methods using numerical 2-D simulations [3], [4]. However, these past efforts of numerical tests to establish regimes of validity were for Gaussian correlation functions. The conclusions of these past tests are not valid for exponential correlation functions.

In this paper, we conduct the numerical Maxwell model with 2-D simulations (NMM2D) for scattering and emission of surfaces with exponential correlation functions. It is well known that exponential correlation functions do not have rms slopes when the spectrum is extended to infinity. In this paper, exponential correlation function surfaces are defined by truncating the spectrum as follows. We generate the random rough surface with exponential correlation function using 1000 points per free space wavelength. This surface is labeled as a "real" exponential correlation function surface as seen by a microwave. Numerical solutions of such exponential surfaces are a challenging task even for 2-D simulations because of the fine irregularities. Numerical accuracies are ensured by a variety of procedures in this paper. Numerical accuracy is important to ensure correct results for emissivity in passive remote sensing as it is related to energy conservation and the accuracy of bistatic scattering coefficients. It is less of a challenge for active monostatic remote sensing as only the backscattering coefficients are calculated in the decibel scale. We found that using the usual method of moments (MoM) procedure of pulse basis functions and point matching can give reasonable results for backscattering coefficients in the decibel scale for small rms height. The former approach gives poor results in emissivity and energy conservation. In this paper, we use the rooftop function and Galerkin's method with numerical integration of near-field impedance matrix elements. A dense discretization of a surface is used. Cubic spline interpolation (CSI) is employed to connect knots on random rough surface. Numerical accuracy convergence tests are performed for numerical solutions of Maxwell equations by varying the number of points from 13 to 103 points per wavelength in the dielectric medium, corresponding to 50–400 points per free wavelength. Energy conservation tests are also conducted. Since we discretize to as many as 400 points

Manuscript received April 22, 2006; revised June 22, 2006. This work was supported in part by Wuhan University under Grant 502-276001, in part by the National Aeronautics and Space Administration, and in part by the Hong Kong RGC under Central Allocation Grant 8730017.

P. Xu is with the School of Electronic Information, Wuhan University, Wuhan 430079, China (e-mail: pxu@whu.edu.cn).

L. Tsang is with the Department of Electrical Engineering, University of Washington, Seattle, WA 98195 USA (e-mail: tsang@ee.washington.edu).

Digital Object Identifier 10.1109/TGRS.2006.883458

per free wavelength, the number of unknowns is more than 80 000 even for a 100-wavelength-long surface. NMM2D simulations are accelerated by the multilevel UV method of matrix solver [5].

In Section II, formulations are given with discretization of MoM equation in terms of rooftop basis functions. The impedance matrix is partitioned. In Section III, CSI is introduced. Convergence is tested by varying the discretization. In Section IV, numerical results including emissivity and bistatic scattering are illustrated at 5 and 10 GHz. Results are compared with the corresponding results of the Gaussian correlation function. Results are also compared with second-order SPM (SPM2) and KA. It is shown that convergences and energy conservation tests are obeyed. The exponential correlation function case has a much larger backscattering than the Gaussian correlation function. It also has a larger emissivity difference from that of a smooth surface. Based on the results of exponential correlation functions, we conclude that KA is invalid at any frequency. SPM2 has bistatic scattering coefficients that are valid for small rms height and invalid for moderate rms height. The SPM2 emissivity results actually do not exist for exponential correlation functions because of divergent spectral integral although the spectral integration can be truncated at a maximum spectral number that results in uncertainties.

## II. GENERAL FORMULATIONS

### A. Discretization of the Integral Equation

Consider a tapered plane wave [5]  $\psi^{\text{inc}}(x, z)$  impinging upon a rough surface with a random height profile  $z = f(x)$ . Let  $\psi$  and  $\psi_1$  denote the wave function for upper medium and lower lossy dielectric media, respectively. Let  $\bar{E} = \hat{y}\psi$  for the TE case and  $\bar{H} = \hat{y}\psi$  for the TM case. We have the dual surface integral equations [3]

$$\int_s dx' g(\bar{r}', \bar{r}) U(\bar{r}') - \int_s ds' \hat{n}' \cdot \psi(\bar{r}') \bar{\nabla}' g(\bar{r}', \bar{r}) + \frac{1}{2} \psi(\bar{r}) = \psi^{\text{inc}}(\bar{r}) \quad (1a)$$

$$\rho \int_s dx' g_1(\bar{r}', \bar{r}) U(\bar{r}') - \int_s ds' \hat{n}' \cdot \psi(\bar{r}') \bar{\nabla}' g_1(\bar{r}', \bar{r}) - \frac{1}{2} \psi(\bar{r}) = 0 \quad (1b)$$

where  $f$  denotes a principle value of integral, and  $g$  and  $g_1$  are the 2-D Green's functions of the upper and lower media, respectively. In (1b),  $\rho = 1$  and  $\varepsilon_1/\varepsilon$  for the TE and TM cases, respectively. Also

$$\psi(\bar{r}) = \psi(x, f(x)) = \psi_1(x, f(x)) \quad (2a)$$

$$U(\bar{r}) = \sqrt{1 + f_x^2} (\hat{n} \cdot \bar{\nabla} \psi(x, f(x))). \quad (2b)$$

Past numerical simulations were done primarily on Gaussian correlation functions. The numerical details and the convergence tests are important to ensure that the results are

accurate for both bistatic scattering coefficients and emissivities. We have used the old approach of pulse basis functions and staircase approximations of the profiles. Both past methods give poor energy conservation. Thus, we use the new numerical approach described below. We use rooftop basis functions

$$F_n(x') = \begin{cases} (x' - x'_{n-1})/(\Delta x'), & \text{for } x'_{n-1} \leq x' < x'_n \\ (x'_{n+1} - x')/(\Delta x'), & \text{for } x'_n \leq x' < x'_{n+1} \end{cases}$$

and Galerkin's method. The integral equations are discretized as

$$\bar{\bar{Z}}_{2N \times 2N} \begin{bmatrix} \bar{U}_{N \times 1} \\ \bar{\psi}_{N \times 1} \end{bmatrix} = \begin{bmatrix} \bar{\bar{A}}_{N \times N}^{(0)} & \bar{\bar{B}}_{N \times N}^{(0)} \\ \bar{\bar{A}}_{N \times N}^{(1)} & \bar{\bar{B}}_{N \times N}^{(1)} \end{bmatrix} \begin{bmatrix} \bar{U}_{N \times 1} \\ \bar{\psi}_{N \times 1} \end{bmatrix} = \begin{bmatrix} \bar{\psi}_{N \times 1}^{\text{inc}} \\ \bar{0}_{N \times 1} \end{bmatrix}. \quad (3)$$

For the sake of accuracy, the near-field impedance matrix elements are calculated by numerical integration. We calculate those elements where  $|n - m| < 20$  by Legendre–Gaussian integration.

For  $|n - m| \geq 20$  we have

$$A_{mn}^{(0)} = \Delta^2 \frac{i}{4} H_0^{(1)}(kR_{nm}) \quad (4a)$$

$$A_{mn}^{(1)} = \Delta^2 \frac{i}{4} H_0^{(1)}(k_1 R_{nm}) \quad (4b)$$

$$B_{mn}^{(0)} = -\Delta^2 \frac{ik}{4} \frac{H_1^{(1)}(kR_{nm})}{R_{nm}} \times [f_{x_n}(x_n - x_m) - (f(x_n) - f(x_m))] \quad (4c)$$

$$B_{mn}^{(1)} = -\Delta^2 \frac{ik_1}{4} \frac{H_1^{(1)}(k_1 R_{nm})}{R_{nm}} \times [f_{x_n}(x_n - x_m) - (f(x_n) - f(x_m))] \quad (4d)$$

where  $\Delta = \Delta x$ , and  $k$  and  $k_1$  are the wavenumbers of the upper and lower media, respectively.  $R_{nm} = \sqrt{(x_n - x_m)^2 + (f_n - f_m)^2}$ , and  $f_{x_n} = (f_{n+1} - f_{n-1})/(2\Delta)$ .

For  $20 > |n - m| > 1$ , integrations are performed by using eight-point Legendre–Gaussian integration

$$A_{mn}^{(0)} = \Delta^2 \frac{i}{4} \sum_{s=1}^8 w_s \sum_{t=1}^8 w_t \left[ \delta_s \delta_t' \sum_{j=1}^4 A_j^{(0)}(\delta_t', \delta_s) \right] \quad (5a)$$

$$A_{mn}^{(1)} = \Delta^2 \frac{i}{4} \sum_{s=1}^8 w_s \sum_{t=1}^8 w_t \left[ \delta_s \delta_t' \sum_{j=1}^4 A_j^{(1)}(\delta_t', \delta_s) \right] \quad (5b)$$

$$B_{mn}^{(0)} = -\Delta^2 \frac{ik}{4} \sum_{s=1}^8 w_s \sum_{t=1}^8 w_t \left[ \delta_s \delta_t' \sum_{j=1}^4 B_j^{(0)}(\delta_t', \delta_s) \right] \quad (5c)$$

$$B_{mn}^{(1)} = -\Delta^2 \frac{ik_1}{4} \sum_{s=1}^8 w_s \sum_{t=1}^8 w_t \left[ \delta_s \delta_t' \sum_{j=1}^4 B_j^{(1)}(\delta_t', \delta_s) \right] \quad (5d)$$

where  $\delta$  is the integral node at zero of Legendre's polynomial,  $w$  is the weight,  $\delta, w \in [0, 1]$ , and

$$\begin{cases} A1_{mn}^{(0)}(\delta', \delta) = H_0^{(1)}(kR(\delta'\Delta + x'_{n-1}, \delta\Delta + x_{m-1})) \\ A2_{mn}^{(0)}(\delta', \delta) = H_0^{(1)}(kR(x'_{n+1} - \delta'\Delta, \delta\Delta + x_{m-1})) \\ A3_{mn}^{(0)}(\delta', \delta) = H_0^{(1)}(kR(\delta'\Delta + x'_{n-1}, x_{m+1} - \delta\Delta)) \\ A4_{mn}^{(0)}(\delta', \delta) = H_0^{(1)}(kR(x'_{n+1} - \delta'\Delta, x_{m+1} - \delta\Delta)) \end{cases} \quad (6)$$

$$\begin{cases} B1_{mn}^{(0)}(\delta', \delta) = \frac{H_1^{(1)}(kR(\Delta\delta' + x'_{n-1}, \Delta\delta + x_{m-1}))}{R(\Delta\delta' + x'_{n-1}, \Delta\delta + x_{m-1})} \\ \quad \times \left[ f_{x_n^-}(\Delta\delta' + x'_{n-1} - (\Delta\delta + x_{m-1})) \right. \\ \quad \left. - (f(\Delta\delta' + x'_{n-1}) - f(\Delta\delta + x_{m-1})) \right] \\ B2_{mn}^{(0)}(\delta', \delta) = \frac{H_1^{(1)}(kR(x'_{n+1} - \Delta\delta', \Delta\delta + x_{m-1}))}{R(x'_{n+1} - \Delta\delta', \Delta\delta + x_{m-1})} \\ \quad \times \left[ f_{x_n^+}(x'_{n+1} - \Delta\delta' - (\Delta\delta + x_{m-1})) \right. \\ \quad \left. - (f(x'_{n+1} - \Delta\delta') - f(\Delta\delta + x_{m-1})) \right] \\ B3_{mn}^{(0)}(\delta', \delta) = \frac{H_1^{(1)}(kR(\Delta\delta' + x'_{n-1}, x_{m+1} - \Delta\delta))}{R(\Delta\delta' + x'_{n-1}, x_{m+1} - \Delta\delta)} \\ \quad \times \left[ f_{x_n^-}(\Delta\delta' + x'_{n-1} - (x_{m+1} - \Delta\delta)) \right. \\ \quad \left. - (f(\Delta\delta' + x'_{n-1}) - f(x_{m+1} - \Delta\delta)) \right] \\ B4_{mn}^{(0)}(\delta', \delta) = \frac{H_1^{(1)}(kR(x'_{n+1} - \Delta\delta', x_{m+1} - \Delta\delta))}{R(x'_{n+1} - \Delta\delta', x_{m+1} - \Delta\delta)} \\ \quad \times \left[ f_{x_n^+}(x'_{n+1} - \Delta\delta' - (x_{m+1} - \Delta\delta)) \right. \\ \quad \left. - (f(x'_{n+1} - \Delta\delta') - f(x_{m+1} - \Delta\delta)) \right] \end{cases} \quad (7)$$

where  $f_{x_n^+} = (f_{n+1} - f_n)/\Delta$ , and  $f_{x_n^-} = (f_n - f_{n-1})/\Delta$ .  $A_{jmn}^{(1)}(\delta', \delta)$  and  $B_{jmn}^{(1)}(\delta', \delta)$  are similar to (6) and (7), respectively, except that  $k$  is replaced by  $k_1$ .

For partial self-patch terms,  $m = n + 1$  we have

$$\begin{aligned} A_{mn}^{(0)} = \Delta^2 \frac{i}{4} \left\{ \frac{1}{4} \left[ 1 + i \frac{2}{\pi} \left( \ln \frac{\gamma k \Delta \sqrt{1 + f_{x_n^+}^2}}{2e} - \frac{1}{4} \right) \right] \right. \\ \left. + \sum_{s=1}^8 w_s \sum_{t=1}^8 w_t \left\{ \delta_s \delta_t' \left[ \sum_{j=1, j \neq 2}^4 A_{jmn}^{(0)}(\delta_t', \delta_s) \right. \right. \right. \\ \left. \left. \left. + \overline{A2}_{mn}^{(0)}(\delta_t', \delta_s) \right] \right\} \right\} \quad (8a) \end{aligned}$$

$$\begin{aligned} A_{mn}^{(1)} = \Delta^2 \frac{i}{4} \left\{ \frac{1}{4} \left[ 1 + i \frac{2}{\pi} \left( \ln \frac{\gamma k_1 \Delta \sqrt{1 + f_{x_n^+}^2}}{2e} - \frac{1}{4} \right) \right] \right. \\ \left. + \sum_{s=1}^8 w_s \sum_{t=1}^8 w_t \left\{ \delta_s \delta_t' \left[ \sum_{j=1, j \neq 2}^4 A_{jmn}^{(1)}(\delta_t', \delta_s) \right. \right. \right. \\ \left. \left. \left. + \overline{A2}_{mn}^{(1)}(\delta_t', \delta_s) \right] \right\} \right\} \quad (8b) \end{aligned}$$

$$B_{mn}^{(0)} = \frac{\Delta}{12} - \Delta^2 \frac{ik}{4} \sum_{s=1}^8 w_s \sum_{t=1}^8 w_t \left[ \delta_s \delta_t' \sum_{j=1, j \neq 2}^4 B_{jmn}^{(0)}(\delta_t', \delta_s) \right] \quad (8c)$$

$$B_{mn}^{(1)} = -\frac{\Delta}{12} - \Delta^2 \frac{ik_1}{4} \sum_{s=1}^8 w_s \sum_{t=1}^8 w_t \left[ \delta_s \delta_t' \sum_{j=1, j \neq 2}^4 B_{jmn}^{(1)}(\delta_t', \delta_s) \right]. \quad (8d)$$

Note that there are different signs between (8c) and (8d), where for  $\delta_t' + \delta_s \neq 1$  we have

$$\begin{cases} \overline{A2}_{mn}^{(0)}(\delta', \delta) = A2_{mn}^{(0)}(\delta', \delta) \\ \quad - \left( 1 + i \frac{2}{\pi} \ln \left( \frac{\gamma}{2} k |1 - \delta' - \delta| \Delta \sqrt{1 + f_{x_n^+}^2} \right) \right) \\ \overline{A2}_{mn}^{(1)}(\delta', \delta) = A2_{mn}^{(1)}(\delta', \delta) \\ \quad - \left( 1 + i \frac{2}{\pi} \ln \left( \frac{\gamma}{2} k_1 |1 - \delta' - \delta| \Delta \sqrt{1 + f_{x_n^+}^2} \right) \right) \end{cases} \quad (9)$$

and while  $\delta_t' + \delta_s = 1$ ,  $\overline{A2}_{mn}^{(0)}(\delta', \delta)$  and  $\overline{A2}_{mn}^{(1)}(\delta', \delta)$  are equal to zero. For  $m = n - 1$ , it is similar to (8) except that  $j \neq 2$  is replaced by  $j \neq 3$  and  $\overline{A2}_{mn}^{(0,1)}$  is replaced by  $\overline{A3}_{mn}^{(0,1)}$ .

For complete self-patch terms,  $m = n$ , as in (10a)–(10d), shown at the bottom of the next page, where for  $\delta_t' \neq \delta_s$  we have

$$\begin{cases} \overline{A1}_{mn}^{(0)}(\delta', \delta) = H_0^{(1)}(kR(x'_{n-1} + \delta'\Delta, x_{n-1} + \delta\Delta)) \\ \quad - \left( 1 + i \frac{2}{\pi} \ln \left( \frac{\gamma}{2} k |\delta' - \delta| \Delta \sqrt{1 + f_{x_n^-}^2} \right) \right) \\ \overline{A4}_{mn}^{(0)}(\delta', \delta) = H_0^{(1)}(kR(x'_{n+1} - \delta'\Delta, x_{n+1} - \delta\Delta)) \\ \quad - \left( 1 + i \frac{2}{\pi} \ln \left( \frac{\gamma}{2} k |\delta' - \delta| \Delta \sqrt{1 + f_{x_n^+}^2} \right) \right) \\ \overline{A1}_{mn}^{(1)}(\delta', \delta) = H_0^{(1)}(k_1 R(x'_{n-1} + \delta'\Delta, x_{n-1} + \delta\Delta)) \\ \quad - \left( 1 + i \frac{2}{\pi} \ln \left( \frac{\gamma}{2} k_1 |\delta' - \delta| \Delta \sqrt{1 + f_{x_n^-}^2} \right) \right) \\ \overline{A4}_{mn}^{(1)}(\delta', \delta) = H_0^{(1)}(k_1 R(x'_{n+1} - \delta'\Delta, x_{n+1} - \delta\Delta)) \\ \quad - \left( 1 + i \frac{2}{\pi} \ln \left( \frac{\gamma}{2} k_1 |\delta' - \delta| \Delta \sqrt{1 + f_{x_n^+}^2} \right) \right) \end{cases} \quad (11)$$

and when  $\delta'_t = \delta_s$ ,  $\overline{A1}_{mn}^{(0)}(\delta'_t, \delta_s) = \overline{A4}_{mn}^{(0)}(\delta'_t, \delta_s) = \overline{A1}_{mn}^{(1)}(\delta'_t, \delta_s) = \overline{A4}_{mn}^{(1)}(\delta'_t, \delta_s) = 0$ .

In addition

$$\psi_m^{\text{inc}} = \int_{x_{m-1}}^{x_{m+1}} dx F_m(x) \psi^{\text{inc}}(\bar{r}). \quad (12)$$

In (3),  $\rho \overline{A}_{N \times N}^{(1)}$  give larger nondiagonal elements for the impedance matrix  $\overline{Z}_{2N \times 2N}$  especially for the TM case, which can create a convergence problem for the TM case at higher frequency. To avoid that, we change (3) into

$$\begin{bmatrix} \overline{B}_{N \times N}^{(0)} & \overline{A}_{N \times N}^{(0)} \\ \overline{B}_{N \times N}^{(1)} & \rho \overline{A}_{N \times N}^{(1)} \end{bmatrix} \begin{bmatrix} \overline{\psi}_{N \times 1} \\ \overline{U}_{N \times 1} \end{bmatrix} = \begin{bmatrix} \overline{\psi}_{N \times 1}^{\text{inc}} \\ \overline{0}_{N \times 1} \end{bmatrix}. \quad (13)$$

Thus,  $\overline{Z}_{2N \times 2N}$  have larger diagonal elements of  $\rho \overline{A}_{N \times N}^{(1)}$ . This gives a better condition number.

### B. Emissivity and Energy Conservation

Emissivity is equal to absorptivity. Absorptivity and reflectivity are calculated by the total and scattered fields on the surface, respectively. For the rooftop, we have

$$\begin{aligned} a(\theta_i) &= \frac{P_a}{P_{\text{inc}}} \\ &= \Delta \frac{\text{Im} \left[ 2 \sum_{n=1}^N \psi_n U_n^* + \frac{1}{2} \sum_{n=1}^N \psi_n (U_{n-1}^* + U_{n+1}^*) \right]}{3k \cos \theta_i G \sqrt{\frac{\pi}{2}} \left( 1 - \frac{1+2 \tan^2 \theta_i}{2k^2 G^2 \cos^2 \theta_i} \right)} \end{aligned} \quad (14a)$$

$$\begin{aligned} r(\theta_i) &= \frac{P_s}{P_{\text{inc}}} \\ &= -\Delta \frac{\text{Im} \left[ 2 \sum_{n=1}^N \psi_n^s U_n^{s*} + \frac{1}{2} \sum_{n=1}^N \psi_n^s (U_{n-1}^* + U_{n+1}^*) \right]}{3k \cos \theta_i G \sqrt{\frac{\pi}{2}} \left( 1 - \frac{1+2 \tan^2 \theta_i}{2k^2 G^2 \cos^2 \theta_i} \right)} \end{aligned} \quad (14b)$$

where  $U_0^* = U_{N+1}^* = U_0^{s*} = U_{N+1}^{s*} = 0$ .  $G$  is the tapering parameter of the incident wave. The surface scattered fields are

$$\psi_n^s = \psi_n - \psi_n^{\text{inc}} \quad (15a)$$

$$\begin{aligned} U_n^s &= U_n - U_n^{\text{inc}} \\ &= U_n - \sqrt{1 + f_{x_n}^2} (\hat{n} \cdot \nabla \psi^{\text{inc}}(x_n, f(x_n))). \end{aligned} \quad (15b)$$

The bistatic scattering coefficient  $\gamma(\theta_s) = 2\pi\sigma(\theta_s)$  is

$$r(\theta_i) = \frac{1}{2\pi} \int_{-\frac{\pi}{2}}^{\frac{\pi}{2}} d\theta_s \gamma(\theta_s) = \int_{-\frac{\pi}{2}}^{\frac{\pi}{2}} d\theta_s \sigma(\theta_s). \quad (16)$$

The backscattering  $\sigma_{\text{back}}$  is

$$\sigma_{\text{back}} = \cos \theta_i \gamma(\theta_s = -\theta_i). \quad (17)$$

In passive remote sensing, the energy conservation test is by showing numerically that  $a(\theta_i) + r(\theta_i) = 1$ . In this paper, the results of  $a(\theta_i) + r(\theta_i)$  are provided for simulations. The bistatic scattering coefficients  $\gamma(\theta_s)$  defined in (16) are illustrated in the plane of incidence with specular scattering direction at the incident angle. For backscattering coefficient, we plot  $\sigma_{\text{back}}$  in the backscattering direction.

### C. Multilevel UV Method [5]

To solve (13), the matrices  $\overline{A}^{(0)}$  and  $\overline{B}^{(0)}$  are partitioned in multilevel as shown in Fig. 1(a), and the near-field interactions, i.e., the zeroth-level submatrices, are further decomposed into the block diagonal part (shaded portions) that is computed directly and the block nondiagonal part (skew line portions) that is compressed by singular-value decomposition (SVD). All subblocks in the far field are compressed with the UV method [5]. Croud's method with partial pivoting is used to

$$\begin{aligned} A_{mm}^{(0)} &= \Delta^2 \frac{i}{4} \left\{ \frac{1}{2} \left[ 1 + i \frac{1}{\pi} \left( 2 \ln \frac{\gamma k \Delta}{2e} + \ln \left( \sqrt{1 + f_{x_n^-}^2} \sqrt{1 + f_{x_n^+}^2} \right) - \frac{3}{2} \right) \right] \right. \\ &\quad \left. + \sum_{s=1}^8 w_s \sum_{t=1}^8 w_t \left\{ \delta_s \delta'_t \left[ \overline{A1}_{mn}^{(0)}(\delta'_t, \delta_s) + 2 \cdot A2_{mn}^{(0)}(\delta'_t, \delta_s) + \overline{A4}_{mn}^{(0)}(\delta'_t, \delta_s) \right] \right\} \right\} \end{aligned} \quad (10a)$$

$$\begin{aligned} A_{mm}^{(1)} &= \Delta^2 \frac{i}{4} \left\{ \frac{1}{2} \left[ 1 + i \frac{1}{\pi} \left( 2 \ln \frac{\gamma k_1 \Delta}{2e} + \ln \left( \sqrt{1 + f_{x_n^-}^2} \sqrt{1 + f_{x_n^+}^2} \right) - \frac{3}{2} \right) \right] \right. \\ &\quad \left. + \sum_{s=1}^8 w_s \sum_{t=1}^8 w_t \left\{ \delta_s \delta'_t \left[ \overline{A1}_{mn}^{(1)}(\delta'_t, \delta_s) + 2 \cdot A2_{mn}^{(1)}(\delta'_t, \delta_s) + \overline{A4}_{mn}^{(1)}(\delta'_t, \delta_s) \right] \right\} \right\} \end{aligned} \quad (10b)$$

$$B_{mm}^{(0)} = \frac{\Delta}{3} - \Delta^2 \frac{ik}{4} \sum_{s=1}^8 w_s \sum_{t=1}^8 w_t \left\{ \delta_s \delta'_t \left[ B2_{mn}^{(0)}(\delta'_t, \delta_s) + B3_{mn}^{(0)}(\delta'_t, \delta_s) \right] \right\} \quad (10c)$$

$$B_{mm}^{(1)} = -\frac{\Delta}{3} - \Delta^2 \frac{ik_1}{4} \sum_{s=1}^8 w_s \sum_{t=1}^8 w_t \left\{ \delta_s \delta'_t \left[ B2_{mn}^{(1)}(\delta'_t, \delta_s) + B3_{mn}^{(1)}(\delta'_t, \delta_s) \right] \right\} \quad (10d)$$

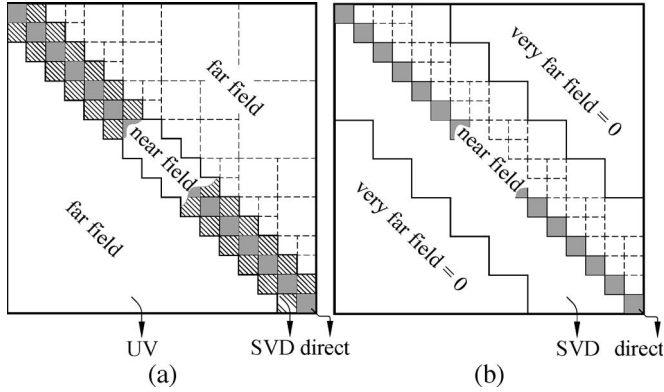


Fig. 1. Impedance matrix partitioning and compression. (a) For  $\overline{\overline{A}}^{(0)}$  and  $\overline{\overline{B}}^{(0)}$  for upper medium. Near field is decomposed into diagonal blocks (direct compute) and nondiagonal blocks (compressed by SVD); far field (compressed by UV) is partitioned into multilevel with dash lines. (b) For  $\overline{\overline{A}}^{(1)}$  and  $\overline{\overline{B}}^{(1)}$  for lossy dielectric medium. Near field is decomposed into diagonal blocks (direct compute) and nondiagonal blocks (compressed by SVD or by UV except for those subblocks adjacent to very far field). The latter is partitioned into multilevel with dash lines. Very far fields are set to zero based on the attenuation in the dielectric medium.

construct matrix  $V$  [6].  $\overline{\overline{A}}^{(1)}$  and  $\overline{\overline{B}}^{(1)}$  are sparse matrices because the Green's functions of the lossy dielectric are attenuative. Those elements that belong to the very far field are exponentially small in the lossy medium and are set equal to zero. The distance range of the very far field depends on the attenuation rate of the lossy dielectric medium. The rest is near field as shown in Fig. 1(b). As for the near field, the block diagonal part is computed directly. The remaining blocks in the near field are compressed by SVD or UV except for those subblocks adjacent to very far field. The inverses of the diagonal blocks of  $\overline{\overline{B}}^{(0)}$  and  $\rho\overline{\overline{A}}^{(1)}$  are used as a preconditioner. In the simulations, we choose  $1e-6$  and  $5e-4$  as thresholds for UV and SVD, respectively. The stabilized biconjugate gradient (BICGstab) method is employed. Iterations are terminated when the error (L2 norm) is less than  $1e-3$ .

### III. GENERATION OF SURFACE AND CONVERGENCE AND ENERGY CONSERVATION TESTS ON EMISSIVITY AND BISTATIC SCATTERING

The spectral density for the exponential correlation function  $W(k_x) = (h^2 l / \pi) \cdot (1 / (1 + k_x^2 l^2))$ . The rms slope of the surface does not exist when one integrates the roughness spectrum to infinity. However, a spectrum to infinity has no physical meaning because a microwave does not "see" features that are less than, for example,  $1/1000$  of its wavelength. In this paper,  $\Delta_0 = 0.006$  cm (i.e., 1000 points per free wavelength at 5 GHz or 500 points per free wavelength at 10 GHz) is used in discretization to generate the "real" rough surface with exponential correlation function. Based on the "real" surface, we can sample points on the "real" surface with different discretization steps (such as  $\Delta_1 = 0.0586$  cm,  $\Delta_2 = 0.0293$  cm, and  $\Delta_3 = 0.0146$  cm, which correspond to 102, 205, and 411 points per free wavelength at 5 GHz and 51, 102, and 205 points per free wavelength at 10 GHz). The relative per-

TABLE I  
RELATIVE PERMITTIVITIES AND WAVELENGTH OF WET SOIL SURFACE AT TWO VOLUMETRIC MOISTURES WITH PARAMETERS: rms  $h = 2.4$  cm, CORRELATION LENGTH  $l = 12$  cm, AND SURFACE LENGTH  $L = 600$  cm

volumetric soil moisture	relative permittivity		$\lambda_1$ (cm)	
	5 GHz	10 GHz	5 GHz	10 GHz
20.0%	$9.09 + i1.43$	$8.88 + i2.63$	1.98	0.996
30.6%	$15.57 + i3.71$	$14.15 + i5.21$	1.51	0.785

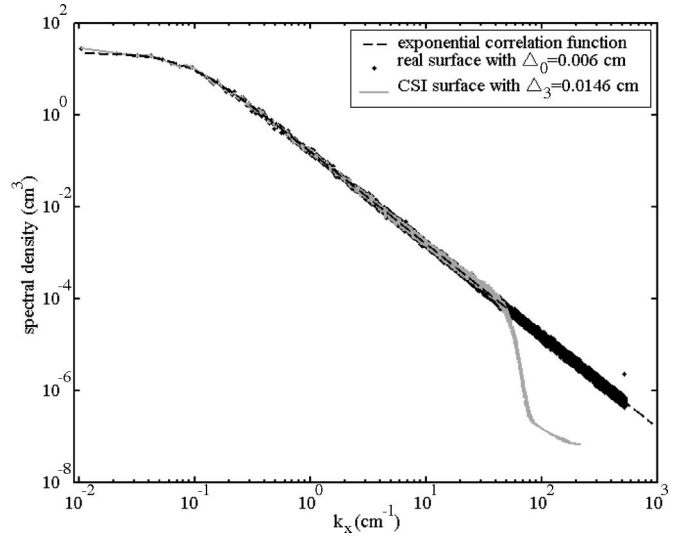


Fig. 2. Comparison of spectral density among exponential correlation function, real surface, and CSI surface averaged over 150 realizations.

mittivities of wet soil for a silt loam with sand of 17.16%, silt of 63.84%, clay of 19.00%, and temperature of  $23^\circ\text{C}$  at 5 and 10 GHz are  $9.09 + i1.43$  and  $8.88 + i2.63$ , respectively, for volumetric moisture  $m_v$  of 20%, and  $15.57 + i3.71$  and  $14.15 + i5.21$ , respectively, for  $m_v$  of 30.6% [7]. The soil physical parameters are also listed in Table I.

The wavelengths in the dielectric medium are  $\lambda_1 = 1.51$  and  $0.785$  cm for volumetric moisture of 30.6% at 5 and 10 GHz, respectively. The discretization corresponds to 26, 52, and 103 points per dielectric medium wavelength at 5 GHz or 13, 27, and 54 points per dielectric medium wavelength at 10 GHz. Apparently, the new surface with  $\Delta_3 = 0.0146$  cm (we call it the third surface) is the closest to the "real" surface. We will use the surface with  $\Delta_3 = 0.0146$  cm as an example to illustrate how it is generated from the "real" surface by using CSI. Step 1: All points where  $x = \dots, -12\Delta_3, -8\Delta_3, -4\Delta_3, 0, 4\Delta_3, 8\Delta_3, 12\Delta_3, \dots$ , are direct points on "real" surface. It can be found that there are three points between each pair of adjacent points, for example, there are points at  $x = -11\Delta_3, -10\Delta_3, -9\Delta_3$  between two points at  $x = -12\Delta_3, -8\Delta_3$ . These points, i.e.,  $x = -11\Delta_3, -10\Delta_3, -9\Delta_3$ , are not direct points on the "real" surface. Step 2: All other points such as  $x = \dots; -11\Delta_3, -10\Delta_3, -9\Delta_3; -7\Delta_3, -6\Delta_3, -5\Delta_3; -3\Delta_3, -2\Delta_3, -\Delta_3; \Delta_3, 2\Delta_3, 3\Delta_3; \dots$  will be generated by CSI based on the direct points data at  $x = \dots, -12\Delta_3, -8\Delta_3, -4\Delta_3, 0, 4\Delta_3, 8\Delta_3, 12\Delta_3, \dots$ . Although some points by CSI on the new surface are not completely coincident with those on the "real" surface, yet when  $\Delta_3$  is small enough, the surface is still close to the real surface.

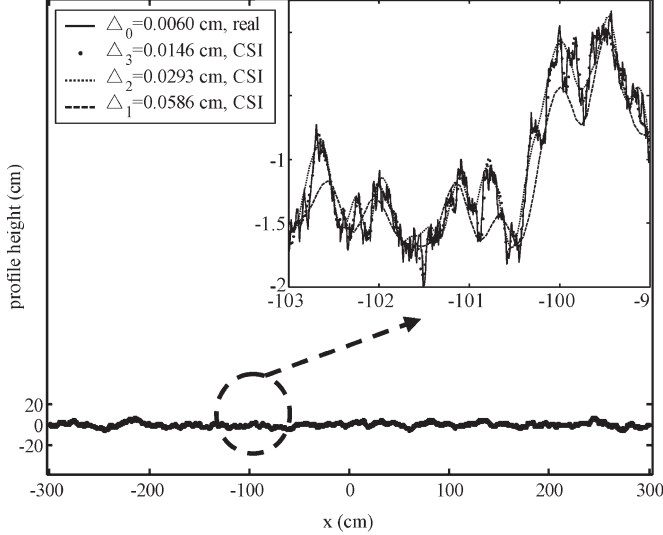


Fig. 3. Profiles with different discretization densities by using CSI compared with a real surface with the exponential correlation function. RMS height  $h = 2.4$  cm, correlation length  $l = 12$  cm, and surface length  $L = 600$  cm.

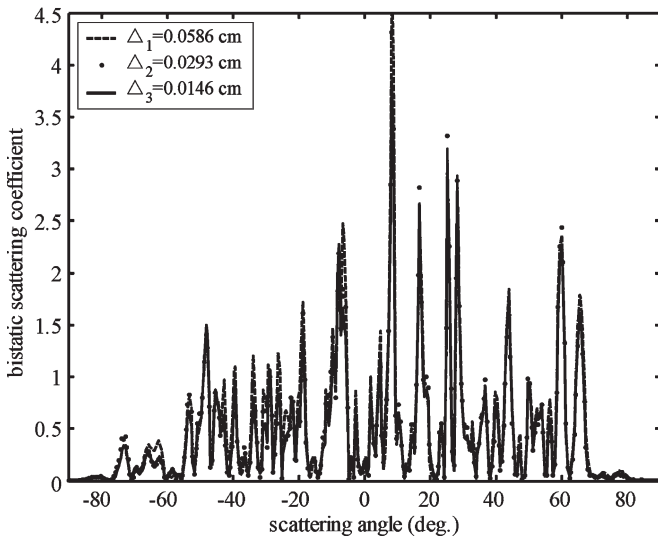


Fig. 4. Comparisons of bistatic scattering coefficients  $\gamma(\theta_s)$  for the TE case with exponential correlation functions among different discretizations. The incident angle  $\theta_i = 40^\circ$ , frequency is of 5 GHz with volumetric moisture  $m_v = 30.6\%$ ,  $h = 2.4$  cm,  $l = 12$  cm, and  $L = 600$  cm.

In Fig. 2, we showed the spectra of the CSI surfaces compared with those of the standard exponential correlation function and that of the “real” surface. The CSI approximates quite well the theoretical spectrum up to a small fraction of a wavelength. Since microwaves do not “see” things much less than its wavelength, we treat the CSI spectrum as acceptable.

Next, we show the convergence of bistatic scattering and emissivities for different discretizations of a single realization of the surface. In the simulations, the tapering parameter of the incident wave is selected to be  $1/4$ . The incident angle is  $40^\circ$  from normal for all cases unless stated otherwise. The BICGstab are stopped with tolerance of less than 0.1%.

Three profiles with exponential correlation functions by using CSI with  $\Delta_1 = 0.0586$  cm,  $\Delta_2 = 0.0293$  cm, and  $\Delta_3 = 0.0146$  cm, respectively, are shown in Fig. 3 compared with the

TABLE II  
COMPARISON OF EMISSIVITIES FOR TE AND TM CASES AT DIFFERENT DISCRETIZATIONS.  $\theta_i = 40^\circ$ , AT 5 GHz WITH  $m_v = 30.6\%$ ,  $h = 2.4$  cm,  $l = 12$  cm,  $L = 600$  cm

polarization	$\Delta$ (cm)	Energy cons.	emissivity	$\Delta$ emiss. (rough-flat)	Emiss. of flat
TE	0.0586	0.9969	0.74264	0.2013	0.54132
	0.0293	0.9977	0.76030	0.2190	
	0.0146	0.9980	0.76811	0.2268	
TM	0.0586	0.9948	0.89239	0.1582	0.73415
	0.0293	0.9943	0.89779	0.1636	
	0.0146	0.9948	0.90285	0.1687	

TABLE III  
MEMORY REQUIREMENT AND CPU OF 1.58-GHz PROCESSOR WITH NUMBER OF UNKNOWN  $2N = 81920$ ,  $h = 2.4$  cm,  $l = 12$  cm,  $L = 600$  cm

Polar.	Memory requirement (MB)	Preprocessing Time (hour)	Number of iterations	Time in CG (s)	Total time (hour)
TE	about 380	5.19	543	3627	6.20
TM	about 380	5.19	201	1420	5.58

“real” surface. The rms height is 2.4 cm, the correlation length is 12 cm, and the surface length is 600 cm.

In Fig. 4, the bistatic scattering for the TE cases at 5 GHz for the three discretizations of the single realization is shown. We can see that scattering results converge with the increase of discretization density. We have also done the TM case for the three discretizations and found also the same convergence trend. In Table II, we list the energy conservation check, the emissivities, and the emissivity differences from that of a smooth surface. We note that energy conservation is obeyed. The emissivities also show convergent results for the different discretization densities.

In Table III, we list the memory requirement and CPU time on a single processor of CPU speed of 1.58 GHz for the case of  $\Delta_3 = 0.0146$  cm. The number of unknowns is  $2N = 81920$ . It can be seen that the CPU is consumed mainly in preprocessing, which includes numerical integration of diagonal blocks, SVD compression for  $\overline{A}^{(1)}$  and  $\overline{B}^{(1)}$ , and the construction of U and V matrices, which consume 2.37, 0.84, and 1.98 h, respectively.

#### IV. NUMERICAL RESULTS AND DISCUSSION

In this section, we illustrate the numerical simulation results of the bistatic scattering coefficients and emissivities. The simulation results described in this section are based on CSI surfaces with  $\Delta_3 = 0.0146$  cm, which were shown to be of sufficient accuracy in the previous section.

##### A. Comparison of Scattering and Emissivity Between Exponential and Gaussian Correlation Functions for a Single Realization

In the past, the Gaussian correlation function has been studied extensively. We compare the bistatic scattering of surfaces between exponential and Gaussian correlation functions for the TE and TM cases, respectively. Because exponential correlation function surfaces have a fine-scale structure, it has larger backscattering. These results are consistent with the previous results of the PEC case [6]. On the other hand,

TABLE IV  
COMPARISON OF EMISSIVITIES FOR TE AND TM CASES BETWEEN  
EXPONENTIAL AND GAUSSIAN CORRELATION FUNCTIONS. AT 5 GHz  
WITH  $m_v = 30.6\%$ ,  $\theta_i = 40^\circ$ ,  $h = 2.4$  cm,  $l = 12$  cm,  $L = 600$  cm

Correlation function	polarization	Energy cons.	Emiss.	$\Delta$ emiss. (rough-flat)	Emiss. of flat
exponential	TE	0.9980	0.76811	0.2268	0.54132
	TM	0.9948	0.90285	0.1713	0.73415
Gaussian	TE	0.9999	0.55848	0.0172	0.54132
	TM	0.9999	0.74219	0.0080	0.73415

the Gaussian correlation function surface has stronger forward scattering. We also list the emissivities in Table IV. The emissivity differences from a smooth surface for exponential correlation function cases are much larger than that of Gaussian correlation functions.

We next study the results of the bistatic scattering coefficients and emissivities by averaging over many realizations. For bistatic scattering, we average over 150 realizations. For emissivity, we only need to average over 20 realizations.

### B. Frequency Dependence

We examine the frequency dependence by comparing the results at 5 and 10 GHz. The parameters at the two frequencies are listed in Table I. The surfaces are both discretized with  $\Delta_3 = 0.0146$  cm (number of surface unknowns  $2N = 81920$ ).

As shown in Fig. 5, we can see that scattering for the TE case is larger than that for the TM case. Along with the increase of frequency, forward scattering decreases for both TE and TM cases. Energy conservations for the TM case at 10 GHz are within 0.8%. The energy conservations for the TE cases are better than the TM cases. The energy conservation at 5 GHz is also better than at 10 GHz. With the increase of volumetric moisture, the scattering coefficients become larger for both polarizations at both frequencies. In Table V, we also show the backscattering  $\sigma_{\text{back}} = \cos \theta_i \gamma(\theta_s = -\theta_i)$  and average emissivity over 20 realizations. Emissivities for rough surface are higher than that of a smooth surface. Emissivities for TE exhibit a larger difference from a smooth surface than that for TM cases. This is because the TM case has the Brewster angle effect and has higher emissivity than the TE case even for a smooth surface. With the increase of frequency, emissivity differences from a smooth surface increase for both TE and TM cases. With the increase of volumetric moisture, the backscattering becomes larger for both TE and TM cases at both frequencies because there is more contrast between air and soil. Emissivities become smaller while emissivity differences from a smooth surface become larger.

In Fig. 6, we show the angular dependence of emissivities at 5 and 10 GHz. For the TE case, emissivities decrease with the increase of observational angle. However, for the TM case, the emissivity for smooth surface increases with the increase of observational angle, while the emissivity of rough surface decreases with the increase of observational angle. The large increases in emissivity for the exponential correlation function surfaces are due to the increase in surface area. The effective surface area seen by the microwaves also increases with frequency as the higher frequency at 10 GHz can see smaller

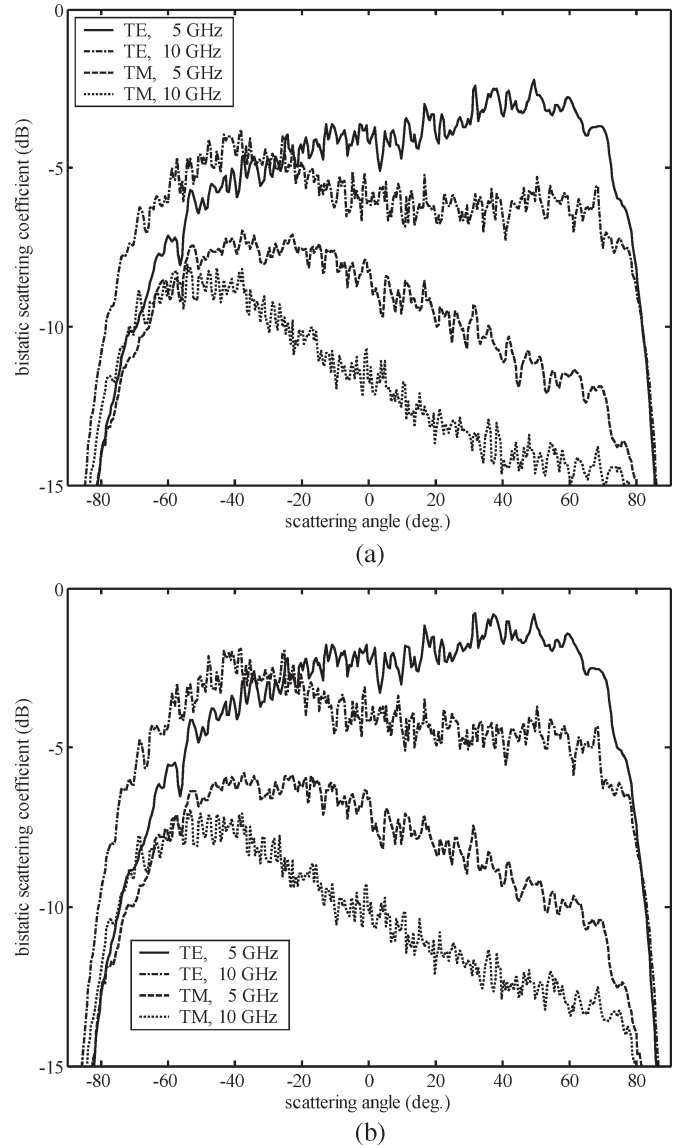


Fig. 5. Average bistatic scattering coefficients  $\gamma(\theta_s)$  from a rough surface with an exponential correlation function with over 150 realizations for both TE and TM cases at 5 and 10 GHz, respectively. For all cases,  $h = 2.4$  cm,  $l = 12$  cm,  $L = 600$  cm,  $\theta_i = 40^\circ$ ,  $\Delta_3 = 0.0146$  cm, and number of surface unknowns  $2N = 81920$ . (a)  $m_v = 20\%$ . (b)  $m_v = 30.6\%$ .

features than 5 GHz. Thus, we also see an increase in emissivity with frequency.

### C. Comparisons With SPM2 and KA

We next compare the results for only the TM case at 5 GHz of both the emissivities and the bistatic scattering coefficients with the SPM2 [8] and the KA. SPM1 refers to the first-order solution of the SPM. The product of two first orders gives the incoherent scattering. Thus, it is customary to just use the first-order fields SPM1 to calculate the incoherent scattering used in active remote sensing. To calculate emissivity in passive remote sensing, one has to go to second order in coherent reflectivity to obtain a result that is consistent with energy conservation, which results in SPM2. Analytic formulas for the SPM2 are given in [8]. Analytical formulas for the KA are given in

TABLE V  
BACKSCATTERING  $\sigma_{\text{back}}$  OVER 150 REALIZATIONS AND AVERAGE EMISSIVITIES OVER 20 REALIZATIONS FROM THE SAME SURFACE WITH THE EXPONENTIAL CORRELATION FUNCTION. FOR ALL CASES,  $h = 2.4$  cm,  $l = 12$  cm,  $L = 600$  cm,  $\theta_i = 40^\circ$ .  
(a)  $m_v = 20\%$ . (b)  $m_v = 30.6\%$

(a)					
polarization	frequency (GHz)	back-scattering (dB)	Emiss.	$\Delta$ emiss. (rough-flat)	Emiss. of flat
TE	5	-6.53	0.83708	0.1860	0.65112
	10	-5.60	0.87434	0.2283	0.64603
TM	5	-8.63	0.93544	0.1031	0.83238
	10	-10.09	0.95201	0.1237	0.82833

(b)					
polarization	frequency (GHz)	back-scattering (dB)	Emiss.	$\Delta$ emiss. (rough-flat)	Emiss. of flat
TE	5	-4.83	0.76577	0.2245	0.54132
	10	-3.56	0.81684	0.2682	0.54869
TM	5	-7.31	0.91447	0.1803	0.73415
	10	-8.87	0.94109	0.1997	0.74139

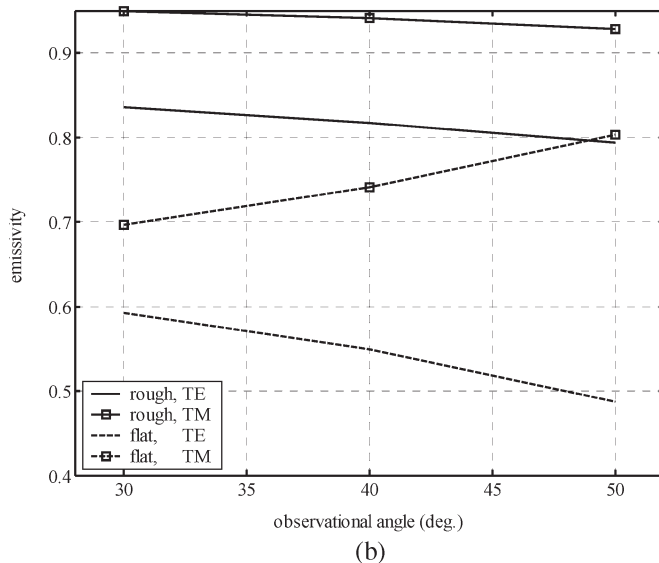
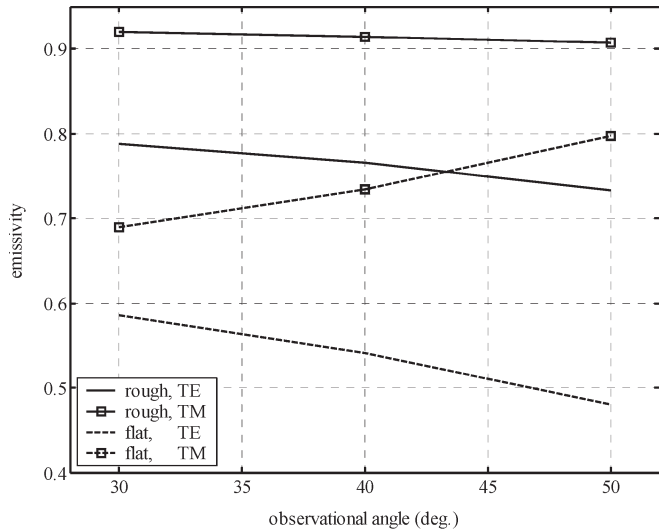


Fig. 6. Emissivity over 20 realizations with exponential correlation function as a function of observational angle.  $h = 2.4$  cm,  $l = 12$  cm,  $L = 600$  cm,  $m_v = 30.6\%$ . (a) At frequency of 5 GHz. (b) At frequency of 10 GHz.

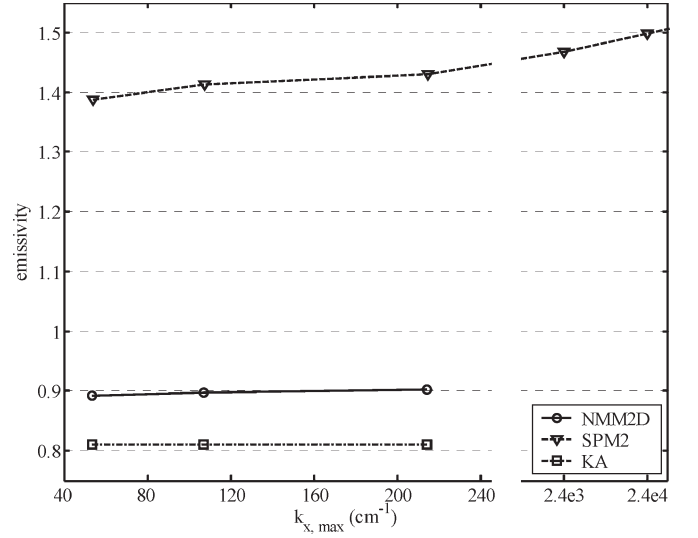


Fig. 7. Comparison of emissivities of exponential correlation function as a function of upper limit of spectrum among NMM2D, SPM2, and KA. For NMM2D, there are three  $k_{x,\text{max}}$  that correspond to  $\Delta_1$ ,  $\Delta_2$ , and  $\Delta_3$ . Parameters: freq = 5 GHz, TM case,  $m_v = 30.6\%$  and  $h = 2.4$  cm,  $l = 12$  cm,  $L = 600$  cm,  $\theta_i = 40^\circ$ .

the Appendix. For SPM2, the incoherent bistatic scattering is plotted. The coherent reflectivity does not actually exist for surfaces with exponential correlation functions because of the divergent spectral integral when integrating over the roughness spectrum variable  $dk_x$  to calculate the coherent reflectivity. However, spectral integration can be truncated at a maximum spectral number, resulting in uncertainties in the computed emissivity values. In Fig. 7, we show the results of emissivities for SPM2, KA, and NMM2D as a function of  $k_{x,\text{max}}$ , indicating the relatively larger uncertainty for SPM2 than NMM2D. Note that at  $k_{x,\text{max}} > 2000$   $\text{cm}^{-1}$ , the SPM2 result further diverges. We make a comparison of the bistatic scattering coefficients in Fig. 8 and emissivities in Table VI for the three cases. For SPM2, we show the result of emissivity by truncating the spectrum at  $k_{x,\text{max}} = 214.5$   $\text{cm}^{-1}$ , which corresponds to  $\Delta_3 = 0.0146$  cm at 5 GHz for NMM2D. The first is with moderate rms height for the Gaussian correlation function. The second is with small rms height for the exponential correlation function. The third one is with moderate rms height for the exponential correlation function. As shown in Fig. 8(a) and Table VI, because of moderate rms height, the scattering by SPM2 is completely different from NMM2D although their emissivities are in good agreement by accident. The bistatic scattering and the emissivity by the KA agree with NMM2D only for surfaces with Gaussian correlation function. As shown in Fig. 8(b) and Table VI, small-scale features in exponential correlation function surfaces still obey Bragg scattering in the low frequency limit, making SPM1 valid for active remote sensing, and if the slope is very small, SPM2 gives reasonable results for passive remote sensing. However, in Fig. 8(c) and Table VI, because of moderate rms height, the results by SPM2 are completely different from NMM2D, not only bistatic scattering. Because the exponential correlation function has fine roughness features, both the scattering and the emissivity by the KA are erroneous and are different from NMM2D. For the third

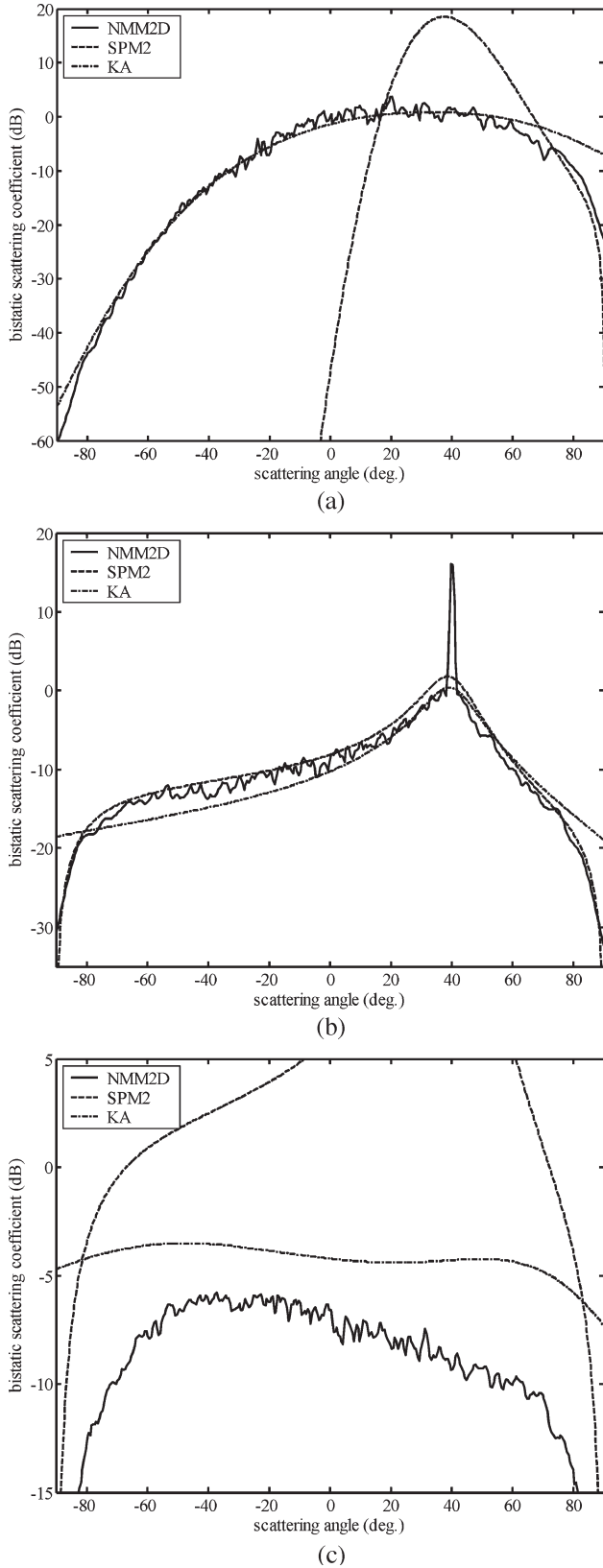


Fig. 8. Comparison of bistatic scattering coefficients  $\gamma(\theta_s)$  for TM by NMM2D with SPM2 and KA for three kinds of surface. For  $m_v = 30.6\%$  with parameters freq = 5 GHz,  $L = 600$  cm, and  $\theta_i = 40^\circ$ . (a) Case of moderate rms height while small slope: Gaussian correlation function,  $h = 2.4$  cm,  $l = 12$  cm. NMM2D over 20 realizations. (b) Case of small rms: exponential correlation function,  $h = 0.4$  cm,  $l = 8.4$  cm. NMM2D over 60 realizations. (c) Case of moderate rms and large slope: exponential correlation function,  $h = 2.4$  cm,  $l = 12$  cm. NMM2D over 150 realizations.

TABLE VI  
COMPARISON OF EMISSIVITY FOR TM BY NMM2D OVER 20 REALIZATIONS WITH SPM AND KA. CASE OF  $m_v = 30.6\%$  WITH PARAMETERS: freq = 5 GHz,  $L = 600$  cm,  $\theta_i = 40^\circ$

Correlation function	$h$ (cm)	$l$ (cm)	emissivity			Emiss. of flat
			NMM2D	SPM2	KA	
Gaussian	2.4	12	0.74245	0.74244	0.74205	0.73415
exponential	0.4	8.4	0.75455	0.76164 <sup>*</sup>	0.73437	
exponential	2.4	12	0.91447	1.42919 <sup>*</sup>	0.81087	

\*integral is actually divergent but with truncated upper limit spectrum  $k_{x,\max} = 214.5 \text{ cm}^{-1}$

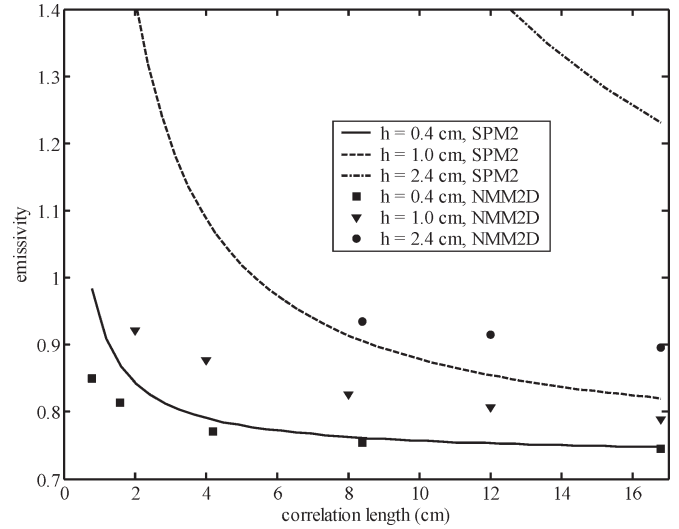


Fig. 9. Emissivity of exponential correlation function by SPM2 and NMM2D over 20 realizations as a function of correlation length for various rms heights by truncating  $k_{x,\max} = 214.5 \text{ cm}^{-1}$ . TM case at 5 GHz,  $m_v = 30.6\%$ .

case with moderate rms height of exponential correlation function, both SPM2 and KA disagree with NMM2D as shown in Fig. 8(c) and Table VI. In Fig. 9, we use SPM2 to plot emissivity as a function of correlation length for various rms heights. To compute SPM2, we truncate at  $k_{x,\max} = 214.5 \text{ cm}^{-1}$ . We also show the results of NMM2D. It is clear that SPM2 agrees with NMM2D only if the rms height to correlation length ratio is extremely small.

For exponential correlation functions, we conclude that KA is invalid at any frequency. The reasons for the failure of KA are that exponential correlation function surfaces have fine scale features. We have not used recent analytic theories such as advanced integral equation model [9], second-order Kirchhoff [10], two-scale model [11], small-slope approximation [12], local curvature approximation [13], etc., as these recent theories are in the evolving stage. The goal of this paper is to obtain benchmark results so that comparisons can be made with analytic theories. Based on the simulations, we make a simple table of comparison showing the contrasts of SPM and KA for Gaussian and exponential correlation functions for active and passive microwave remote sensing. By active remote sensing, we only refer to monostatic backscattering coefficients at small to moderate angles of incidence. Since KA is not valid at any frequency, it may not be worthwhile to develop a theory to bridge the gap between SPM and KA for the exponential correlation function as was done in the case of the Gaussian correlation function. We state in Table VII that SPM2 is not

TABLE VII  
NEW VALIDITY CONDITIONS COMPARING THE TRADITIONAL  
VIEWPOINTS AND NEW VIEWPOINT CONCERNING  
EXPONENTIAL CORRELATION FUNCTIONS

Case	Gaussian	Exponential
Active monostatic: low frequency	SPM1 valid, KA1 not valid	SPM1 valid, KA1 not valid
Active monostatic: high frequency	SPM1 not valid, KA1 valid	SPM1 not valid, KA1 not valid
Passive: low frequency	SPM2 valid if slope is small, KA1 not valid	SPM2 not valid, KA1 not valid
Passive: high frequency	SPM 2 valid if slope is small, KA1 valid	SPM2 not valid, KA1 not valid

valid for passive unless the rms height to correlation length ratio is small. The fine-scale features act as strong diffuse scatterers. The large slopes correspond to larger surface length, making absorption larger.

## V. CONCLUSION

Accurate simulations for the 2-D scattering problem with an exponential correlation function are obtained with the rooftop basis function and Galerkin's method. The multilevel UV method is employed to accelerate the MoM solution. Near-field integration, fine discretization, and cubic spine interpolation of surfaces are used. Numerical results converge with varying discretization densities and are validated by energy conservation tests. Results are illustrated using parameters in microwave remote sensing of soil moistures [14].

## APPENDIX KA

Derivations are similar to [15]. The bistatic scattering coefficient for the incoherent TM wave is

$$\sigma_{\text{incoh}}(\theta_s) = \frac{k \cos^2 \theta_s}{\cos \theta_i} J(k_x) \quad (\text{A1})$$

where

$$J(k_x) = \left| \frac{k_{dx} k_{ix} - k_{iz} k_{dz}}{k_z k_{dz}} R_v^{(0)} \right|^2 \exp(-k_{dz}^2 h^2) \times \sum_{m=1}^{\infty} \frac{(k_{dz}^{2m})}{m!} W^{(m)}(-k_{dx}) \quad (\text{A2})$$

$$\begin{cases} k_x = k \sin \theta_s \\ k_z = k \cos \theta_s \end{cases} \quad \begin{cases} k_{ix} = k \sin \theta_i \\ k_{iz} = k \cos \theta_i \end{cases}$$

$$\begin{cases} k_{dx} = k_{ix} - k_x \\ k_{dz} = -k_{iz} - k_z \end{cases} \quad \begin{cases} k_{1z} = \sqrt{k_1^2 - k_x^2} \\ k_{1iz} = \sqrt{k_1^2 - k_{ix}^2} \end{cases}$$

$R_v^{(0)}$  is the Fresnel reflection coefficient at  $\theta_i$

$$R_v^{(0)} = (\rho k_{iz} - k_{1iz}) / (\rho k_{iz} + k_{1iz}) \quad (\text{A3})$$

and  $W^{(m)}(-k_{dx})$  is the  $m$ th-order spectrum

$$W^{(m)}(-k_{dx}) = \begin{cases} \frac{h^{2m} l}{2\sqrt{m\pi}} \exp\left(-\frac{k_{dx}^2 l^2}{4m}\right), & \text{for Gaussian correlation} \\ \frac{mh^{2m} l}{\pi(m^2 + k_{dx}^2 l^2)}, & \text{for exponential correlation.} \end{cases} \quad (\text{A4})$$

The emissivity is

$$e(\theta_i) = 1 - r_{\text{coh}} - r_{\text{incoh}} \quad (\text{A5})$$

where

$$r_{\text{coh}} = \left| R_v^{(0)} \right|^2 \exp(-4k_{iz}^2 h^2) \quad (\text{A6})$$

$$r_{\text{incoh}} = \int_{-\frac{\pi}{2}}^{\frac{\pi}{2}} d\theta_s \sigma_{\text{incoh}}(\theta_s). \quad (\text{A7})$$

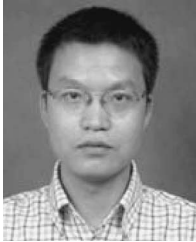
## ACKNOWLEDGMENT

The authors would like to thank G. Q. Zhu and H. Y. Ke (Wuhan University) for computational facilities.

## REFERENCES

- [1] Q. Li, M. Y. Xia, L. Tsang, L. Zhou, C. H. Chan, and Z. X. Li, "Rough surface scattering: Numerical simulations and applications in microwave remote sensing," in *Wiley Encyclopedia on RF and Microwave Engineering*, vol. 5. Hoboken, NJ: Wiley, 2005, pp. 4549–4584.
- [2] L. Zhou, L. Tsang, V. Jandyala, Q. Li, and C. H. Chan, "Emissivity simulations in passive microwave remote sensing with 3-D numerical solutions of Maxwell equations," *IEEE Trans. Geosci. Remote Sens.*, vol. 42, no. 8, pp. 1739–1748, Aug. 2004.
- [3] L. Tsang, J. A. Kong, and R. Shin, *Theory of Microwave Remote Sensing*. New York: Wiley, 1985.
- [4] A. Ishimaru, *Wave Propagation and Scattering in Random Media*. New York: Academic, 1978.
- [5] L. Tsang, D. Chen, P. Xu, Q. Li, and V. Jandyala, "Wave scattering with the UV multilevel partitioning method: 1. Two-dimensional problem of perfect electric conductor surface scattering," *Radio Sci.*, vol. 39, no. 5, Oct. 2004. RS5010.
- [6] P. Xu and L. Tsang, "Scattering by rough surface using a hybrid technique combining the multilevel UV method with the sparse matrix canonical grid method," *Radio Sci.*, vol. 40, no. 4, Aug. 2005. RS4012.
- [7] M. T. Hallikainen, F. T. Ulaby, M. C. Dobson, M. A. El-Rayes, and L. K. Wu, "Microwave dielectric behavior of wet soil—Part I: Empirical models and experimental observations," *IEEE Trans. Geosci. Remote Sens.*, vol. GE-23, no. 1, pp. 25–34, Jan. 1985.
- [8] X. Gu, L. Tsang, H. Braunisch, and P. Xu, "Modeling absorption of rough interface between dielectric and conductive medium," *Microw. Opt. Technol. Lett.*, vol. 49, no. 1, pp. 7–13, Jan. 2007.
- [9] K. S. Chen, T. D. Wu, L. Tsang, Q. Li, J. Shi, and A. K. Fung, "Emission of rough surfaces calculated by the integral equation method with comparison to three-dimensional moment method simulations," *IEEE Trans. Geosci. Remote Sens.*, vol. 41, no. 1, pp. 90–101, Jan. 2003.
- [10] A. Ishimaru and J. S. Chen, "Scattering from very rough surfaces based on the modified second-order Kirchhoff approximation with angular and propagation shadowing," *J. Acoust. Soc. Amer.*, vol. 88, no. 4, pp. 1877–1883, 1990.
- [11] W. J. Plant, "A two-scale model of short wind-generated waves and scatterometry," *J. Geophys. Res.*, vol. 91, no. C9, pp. 10735–10749, Sep. 1986.
- [12] A. Voronovich, "Small-slope approximation for electromagnetic wave scattering at a rough interface of two dielectric half-space," *Wave Random Media*, vol. 4, no. 3, pp. 337–367, Jul. 1994.

- [13] T. Elfouhaily, S. Guignard, R. Awadallah, and D. R. Thompson, "Local and non-local curvature approximation: A new asymptotic theory for wave scattering," *Waves Random Media*, vol. 13, no. 4, pp. 321–337, Oct. 2003.
- [14] E. G. Njoku and L. Li, "Retrieval of land surface parameters using passive microwave sensing at 6–18 GHz," *IEEE Trans. Geosci. Remote Sens.*, vol. 37, no. 1, pp. 79–93, Jan. 1999.
- [15] L. Tsang, J. A. Kong, and K. H. Ding, *Scattering of Electromagnetic Waves: Theories and Applications*. New York: Wiley, 2000, pp. 407–416.



**Peng Xu** received the B.S. degree in applied chemistry from Tianjin University, Tianjin, China, in 1993, and the M.S. and Ph.D. degrees in radio physics from Wuhan University, Wuhan, China, in 2000 and 2005, respectively.

In 2003, he was with the Department of Electronic Engineering, City University of Hong Kong, as a Research Associate and was promoted to Senior Research Associate in 2004. Since 2005, he has been a Lecturer with the School of Electronic Information, Wuhan University. His research interests include computational electromagnetics, microwave remote sensing, and rough surfaces.



**Leung Tsang** (S'73–M'75–SM'85–F'90) received the S.B., S.M., and Ph.D. degrees from the Massachusetts Institute of Technology, Cambridge.

He is a Professor and the Associate Chairman for Education with the Electrical Engineering Department, University of Washington, Seattle, where he has taught since 1983. Between 2001 and 2004, while on leave, he was the Chair Professor and Assistant Head with the Department of Electronic Engineering, City University of Hong Kong. He is the author of four books, namely *Theory of Microwave Remote Sensing*, *Scattering of Electromagnetic Waves, Vol. 1: Theory and Applications*, *Scattering of Electromagnetic Waves, Vol. 2: Numerical Simulations*, and *Scattering of Electromagnetic Waves, Vol. 3: Advanced Topics*. His current research interests include remote sensing and geoscience applications, multiple scattering of waves, signal integrity, computational electromagnetics, and wireless communications.

Dr. Tsang has been the President of the IEEE Geoscience and Remote Sensing Society (GRSS) since January 2006. He was the Editor-in-Chief of the IEEE TRANSACTIONS ON GEOSCIENCE AND REMOTE SENSING from 1996 to 2001. He was the General Chairman of the 1998 IEEE International Geoscience and Remote Sensing Symposium. He received the IEEE GRSS Outstanding Service Award in 2000. He was the recipient of the IEEE Third Millennium Medal in 2000. He is a Fellow of the Optical Society of America.